PCCP

PAPER

View Article Online
View Journal | View Issue

Cite this: *Phys. Chem. Chem. Phys.*, 2015, **17**, 5352

Elucidating the real-time Ag nanoparticle growth on α-Ag_2WO_4 during electron beam irradiation: experimental evidence and theoretical insights†

Wyllamanney da Silva Pereira,[a] Juan Andrés,*[b] Lourdes Gracia,[b] Miguel A. San-Miguel,[c] Edison Z. da Silva,[d] Elson Longo[e] and Valeria M. Longo[f]

Received 13th December 2014,
Accepted 9th January 2015

DOI: 10.1039/c4cp05849f

www.rsc.org/pccp

Why and how Ag is formed when electron beam irradiation takes place on α-Ag_2WO_4 in a vacuum transmission electron microscopy chamber? To find an answer, the atomic-scale mechanisms underlying the formation and growth of Ag on α-Ag_2WO_4 have been investigated by detailed *in situ* transmission electron microscopy (TEM) and field emission scanning electron microscopy (FE-SEM) studies, density functional theory based calculations and *ab initio* molecular dynamics simulations. The growth process at different times, chemical composition, size distribution and element distribution were analyzed in depth at the nanoscale level using FE-SEM, operated at different voltages (5, 10, 15, and 20 kV), and TEM with energy dispersive spectroscopy (EDS) characterization. The size of Ag nanoparticles covers a wide range of values. Most of the Ag particles are in the 20–40 nm range. The nucleation and formation of Ag on α-Ag_2WO_4 is a result of structural and electronic changes in the AgO_x (x = 2,4, 6, and 7) clusters used as constituent building blocks of this material, consistent with metallic Ag formation. First principle calculations point out that Ag-3 and Ag-4-fold coordinated centers, located in the sub-surface of the (100) surface, are the most energetically favorable to undergo the diffusion process to form metallic Ag. *Ab initio* molecular dynamics simulations and the nudged elastic band (NEB) method were used to investigate the minimum energy pathways of these Ag atoms from positions in the first slab layer to outward sites on the (100) surface of α-Ag_2WO_4. The results point out that the injection of electrons decreases the activation barrier for this diffusion step and this unusual behavior results from the presence of a lower energy barrier process.

1. Introduction

An important branch of modern science is devoted to the study of a quantum phenomenon associated with the interaction of electron irradiation and electromagnetic radiation with matter. Predicting the response of a material to the passage of electrons and waves is a very challenging problem. The understanding of spatial scales of atoms and chemical bonds and of temporal scales of electron and nuclear motion has gained increasing sophistication through the development of precise photon and electron probes. The physical and chemical properties of a material are determined by the type of motion its electrons are allowed to execute. Therefore, the ultimate goal is to resolve the fundamental temporal and spatial scales of electron and nuclear motion.

A free electron exerts a force on a nanostructure as it approaches. At long distances this is primarily a Coulomb type interaction but when the electron enters the region of charge density it becomes indistinguishable from the nanomaterial electrons so that additional quantum mechanical exchange interactions become effective. The irradiation of electrons induces the presence of hot (unbound or unconfined) electrons that are not quantized and can thus absorb any amount of energy, modifying the physical and chemical properties of the material. Despite the importance of this phenomenon, the fundamental physical picture is still unclear, and an understanding of the electronic rearrangement processes is mandatory.

Transmission electron microscopy (TEM) and field emission scanning electron microscopy (FE-SEM) are well recognized

[a] *INCTMN-UFSCar, Universidade Federal de São Carlos, P.O. Box 676, 13565-905 São Carlos, SP, Brazil. E-mail: wyllamanneysp@gmail.com*
[b] *Departament de Química Física i Analítica, Universitat Jaume I (UJI), Castelló 12071, Spain. E-mail: andres@qfa.uji.es, lgracia@qfa.uji.es*
[c] *Institute of Chemistry, University of Campinas - Unicamp, 13083-970, Campinas, SP, Brazil. E-mail: smiguel@iqm.unicamp.br*
[d] *Institute of Physics "Gleb Wataghin", University of Campinas - Unicamp, 13083-970, Campinas, SP, Brazil. E-mail: zacarias@ifi.unicamp.br*
[e] *INCTMN-UNESP, Universidade Estadual Paulista, P.O. Box 355, CEP 14801-907 Araraquara, SP, Brazil. E-mail: elson.liec@gmail.com*
[f] *INCTMN-USP, Universidade de São Paulo, Instituto de Física de São Carlos, 13560-970 São Carlos, SP, Brazil. E-mail: lelalongo@icloud.com*

† Electronic supplementary information (ESI) available. See DOI: 10.1039/c4cp05849f

techniques that provide unique capabilities for *in situ* imaging and control of nanoscale phenomena.[1–5] They provide, at the same time, morphological and crystallographic information such as the size and shape of the nanoparticles, the crystallographic phase, the arrangement of atoms in the specimen, and their degree of order.[6–9] The effects introduced with an electron beam of a TEM are directly analyzed from the produced TEM images, and the analysis on the scattering of the electrons that exit the back surface of the specimen provides much microstructure/electronic structure information on the samples based on a variety of electron–solid interaction mechanisms. Therefore, the direct observation of the structures is a powerful scientific tool in material science and provides dynamic information on the solid surface, which cannot be obtained directly by other *in situ* techniques.[7]

Different research groups have utilized the electron beam to promote the chemical precipitation of nanoparticles from solution,[2,10–12] and to induce the deposition of metals and semiconductors from various precursors.[13–15] The role of the electron beam in affecting the chemical reactions has been analyzed.[2,16] A wide variety of metal nanoparticles with different morphologies have also been synthesized and characterized by electron microscopy.[17–25] Some reviews of these syntheses and related processes involving electron energy loss experiments have been published.[26,27] In these studies an electron beam is used for structural and morphological characterization, and can be used to carry out dynamic *in situ* experiments.[28] In particular, the development of liquid cells for TEM has enabled dynamic information about nanosystems and the direct observation of nanoparticle growth in a liquid phase.[1,29,30]

The effect *in vacuo* is quite different since the liquids have a strong influence on their physical and chemical properties. During imaging, the electron beam interacts with the sample, and different research groups have reported on nanoscale crystallization and growth processes taking place only in the beam's presence.[2,10,12,16,30–32] Specifically, plasmonic noble metal nanocrystals have recently been found to enhance a number of chemical reactions due to localized surface plasmon resonances.[33–45] However, the nature of the mechanism of the plasmonic driven chemistry in the presence of hot electrons or charged species and the concurrent photoluminescence properties over plasmonic particles are not well understood.[33,37,46,47]

This investigation's motivation essentially arises from the discovery of an unwanted real-time *in situ* nucleation and growth of Ag filaments on α-Ag_2WO_4 crystals which was driven by an accelerated electron beam from an electronic microscope under high vacuum.[48,49] This is the first example of such studies in the scientific literature and it has become a major topic in current research. It is a novel example of dynamic single crystals where electron irradiation induces macroscopic mobility presenting a visually appealing demonstration of their potential as a bactericide and in photoluminescent applications,[50,51] as well as their application as an efficient ozone sensor.[52] But, they also provide a unique opportunity to explore the mechanistic link between collective atomic processes and their consequences at a macroscopic level. This phenomenon is of an electron-driven nature. The key difference in this approach is the use of an electron beam of TEM for growing Ag nanoparticles rather than for optical or electromagnetic erasing as is the case in the plasmon effect. The knowledge of the driving force and origin of this phenomenon is of utmost importance.

An electron beam was used to grow Ag nanoparticles from α-Ag_2WO_4 crystals. TEM and field emission scanning electron microscopy (FE-SEM) were used to study these materials. The growth process (at different times), chemical composition, size distribution and element distribution were analyzed in depth at the nanoscale level using FE-SEM, operated at different voltages (5, 10, 15, and 20 kV), and TEM with energy dispersive spectroscopy (EDS) characterization. First principle calculations are essential in understanding the experimental observations and for gaining a more complete understanding of this intricate mechanism at atomic levels. First principles density functional theory (DFT) calculations have been carried out to obtain a better understanding of the processes that occur during the initial stages of Ag nanoparticle formation. This present work can be considered a combination of experimental and theoretical studies based on the results obtained by experimental techniques and calculations carried out using the DFT method in order to provide a deeper understanding of atomic and electronic structures associated with the formation of Ag, which was followed by a subsequent nano- to micro-scale growth process.

The research discussed in the present study provides a convenient example of a ''complex modeling paradigm'', introduced by Billinge and Levin,[53] as an appropriate procedure for combining the results of multiple experimental methods and theory in a self-consistent computational framework leading to a greater understanding of this process. Four sections complete this article. The Experimental procedure details are presented in Section 2. The Computational details are given in Section 3. In Section 4, Experimental and theoretical results are presented and discussed in detail. A brief summary and the main conclusions will be offered in the final section.

2. Experimental procedure

Synthesis of α-Ag_2WO_4

α-Ag_2WO_4 microcrystals were prepared at 358 K for 30 min by a simple precipitation method without the use of any surfactant. The typical synthesis procedure of α-Ag_2WO_4 crystals is described as follows: 1×10^{-3} mol of tungstate sodium dihydrate ($Na_2WO_4 \cdot 2H_2O$; 99.5% purity, Sigma-Aldrich) was dissolved in 5 mL of deionized water and 2×10^{-3} mol of silver nitrate ($AgNO_3$; 99.8% purity, Sigma-Aldrich) was dissolved in 95 mL of deionized water at 358 K. The tungstate solution was added to the silver solution with stirring. The resulting suspensions were washed with deionized water and acetone several times to remove remaining ions and dried at 60 °C for 12 h.

Experimental characterization of α-Ag_2WO_4

The α-Ag_2WO_4 crystals were structurally characterized by X-ray diffraction (XRD) patterns using a diffractometer model LabX

XRD-6000 (Shimadzu®, Japan) with Cu-Kα radiation (λ = 1.5406 Å) in the 2θ range from 10° to 70° with a scanning velocity of 1° per min. The shapes, sizes, visualization of Ag filaments and element distribution of the α-Ag_2WO_4 microcrystals were observed using a FEG-SEM model Supra 35-VP, Carl Zeiss, Germany operated at 5, 10, 15 and 20 kV, and a TEM operating at 200 KV and an EDS, model Tecnai G2TF20, FEI.

3. Computational details

Periodic DFT based calculations were performed using the VASP code.[54–56] The valence electrons are described using a plane wave basis set and the effect of the inner cores on the valence electron density is taken into account using the projector augmented wave (PAW) method.[57,58] The valence states that are explicitly included in the calculation are 5d and 6s (6 electrons) for W, 4d and 5s (11 electrons) for Ag atoms, and 2s and 2p (6 electrons) for O atoms. The rest of the electrons are considered as core electrons and their densities are kept frozen as in the reference used to extract the PAW potential.[57,58] A kinetic energy cutoff of 460 eV for the plane wave expansion is used for all systems, which is adequate to obtain total energies converged to at least 1 meV per atom.

The Brillouin zone was sampled using the Monkhorst–Pack method and at different *k*-point grids according to the system size. The number of *k*-points was increased for the analysis of the electronic structure with respect to the geometry optimization process and the tetrahedron method with Blöchl corrections[59] was also used. All calculations were non-spin-polarized. The generalized gradient approximation (GGA) in the Perdew–Burke–Ernzerhof (PBE) formulation was used for the electron exchange and correlation contribution to the total energy.[60,61] The conjugated gradient (CG) energy minimization method was used to obtain relaxed systems. Atoms are considered to be fully relaxed when the Hellmann–Feynman forces converged to less than 0.005 eV per Å per atom.

Ab initio molecular dynamics simulations were performed in selective cases in the canonical ensemble at 300 K. The time step was 3 fs, and a typical simulation spanned about 3 ps. The nudged elastic band (NEB) method was used to investigate the minimum energy pathways of the Ag atoms from positions in the first slab layer to outward sites on the nanoparticle surface. Both the initial and end point configurations were previously optimized. Then intermediate configurations were generated by a linear interpolation between the initial and end points. Finally, the intermediate configurations were relaxed under the constraint that the ions were connected by springs to keep them equidistant from neighboring configurations. Details of the NEB method are described by Jonsson *et al.*[62]

4. Results and discussion

Fig. 1 shows the XRD patterns. All of the diffraction peaks of samples can be assigned to the orthorhombic α-Ag_2WO_4 crystals with a space group *Pn2n* (JCPDS card No. 4165), and the strong

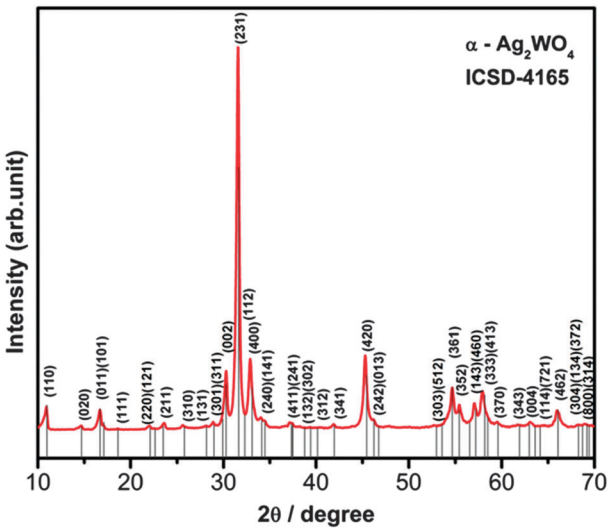

Fig. 1 XRD pattern of an α-Ag_2WO_4 sample.

diffraction peaks revealed crystallinity. The sample was totally monophased α-Ag_2WO_4, in good agreement with previous observations in neutral[63–66] or slightly alkaline[67] media. In α-Ag_2WO_4 crystals, Ag ions can display different AgO_x clusters corresponding to type-coordination and synergistic coordination modes in order to facilitate the formation of several clusters with low and high coordination numbers (x = 2, 4, 6 and 7).

The TEM image in Fig. 2 clearly demonstrates the formation of Ag nanoparticles on α-Ag_2WO_4 microrods at different times (from 0 to 5 minutes). Some nanoparticles assemble into flower-like aggregates. The rod surface is observed to be smooth.

Fig. 3(A–H) shows a FE-SEM image of the crystals that were obtained after a rapid approach and focus adjustment (time zero) at 5, 10, 15 and 20 kV, during the growth of Ag when stimulated by the electron beam on the α-Ag_2WO_4 surface. Further information on the Ag growth process can be found in the ESI.†

This phenomenon occurs after a few seconds of exposure. An analysis of the images reveals increasing formation of Ag

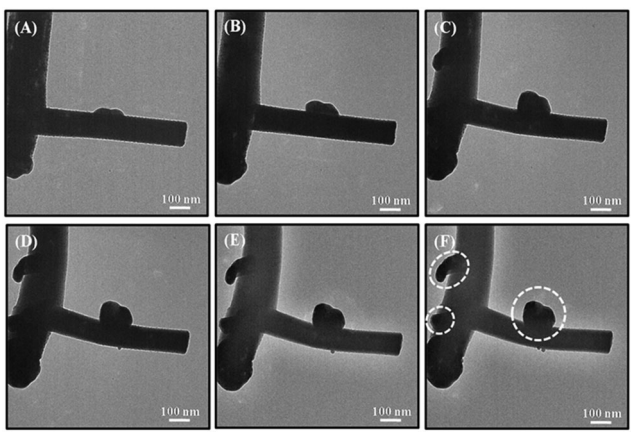

Fig. 2 TEM images of an α-Ag_2WO_4 sample obtained at (A) time zero, (B) 1 min, (C) 2 min, (D) 3 min, (E) 4 min and (F) 5 min of exposure to the electron beam. Ag nanoparticles appear in the middle of both microrods.

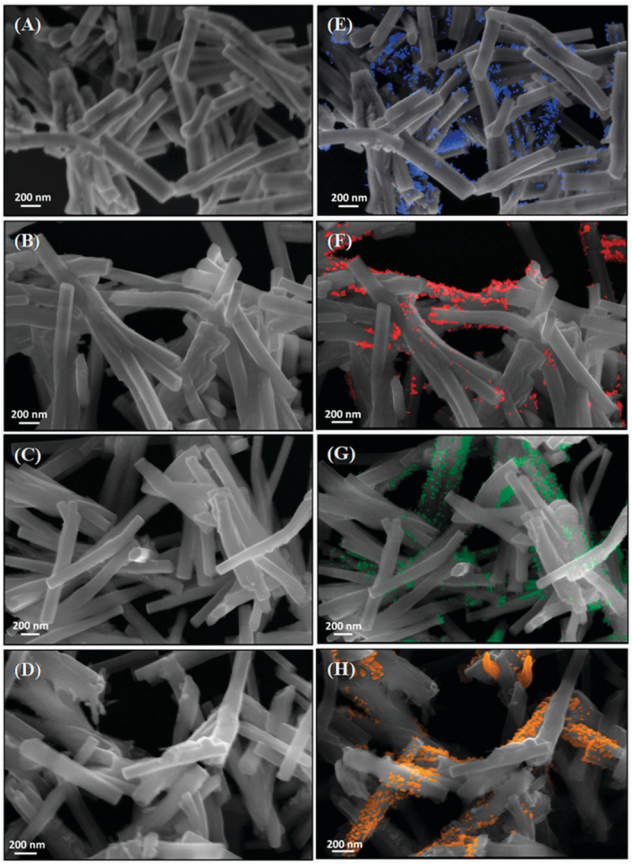

Fig. 3 Time-resolved FE-SEM images of α-Ag_2WO_4 operated at different voltages (A and E) 5 kV, (B and F) 10 kV, (C and G) 15 kV, and (D and H) 20 kV. A–D images were obtained at zero time while E–H images are displayed after 5 min of exposure to the electron beam.

nanoparticles on the surface with an increase in voltage. The size distribution of the Ag nanoparticles at different voltages for 5 minutes has been obtained and the results are displayed in Fig. 4. Different configurations can be formed during the rapid growth of Ag nanoparticles generating Ag vacancy defects, which can be responsible for the different average particle size distributions. An analysis of the results shows two important facts. The first is related to the distribution range that increases with the increase in time and the second is that the nanoparticle size increases with an increase in voltage.

In this typical semiconductor, the electronic structure of the α-Ag_2WO_4 microcrystal is governed by both inter-clusters (intermediary range) and intra-clusters (local range) of the cluster constituents of this material, AgO_2, AgO_4, AgO_6, and AgO_7, and the electron–hole pairs are produced in these clusters. When the electrons hit the surface, the oxidation of stoichiometric Ag_2WO_4 into non-stoichiometric $Ag_{2-x}WO_4$ can accelerate the generation of LSPRs.[68,69] All of these LSPRs are based on the tunable hole concentration induced by the Ag vacancies in the Ag_2WO_4 surface. This perspective addresses the exciting fundamental opportunities arising from the plasmon resonances of semiconductors. The LSPR can be considered, in the most general sense, as an optical signature of any arbitrary

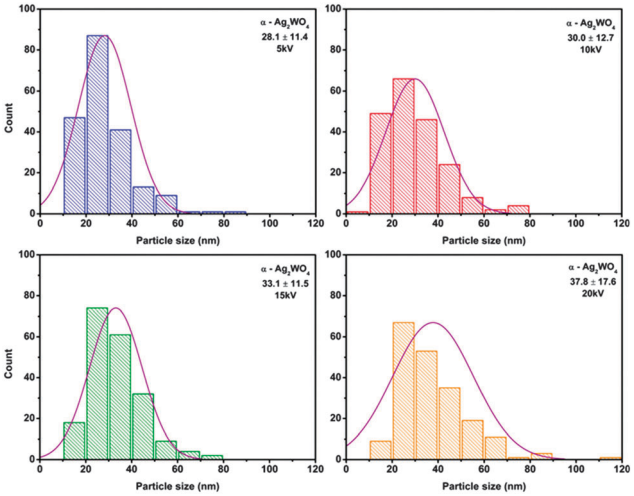

Fig. 4 Mean particle diameter distribution at 5 minutes of electron beam exposure for different voltages. Violet curves are normal fits.

collection of charge carriers. It is not essential for the arbitrary collection of charge carriers. It is not essential for these charges to have purely free character.[20,70–72]

Fig. 5 illustrates the TEM images with EDS characterization. The composition results are shown in Table 1. Therefore, the end of the region that emerged due to the electron exposure (point 1) confirmed the composition of 100% Ag in relation to W. It is possible to see the crystallographic planes revealing the Ag crystallinity. The region near the interface, point 2, is composed of about 92.5% Ag and 7.5% W; while, the internal region, point 3, shows 96.9% W. These results reinforce the fact that the Ag atoms come from the interior deep regions of the particles. This behavior

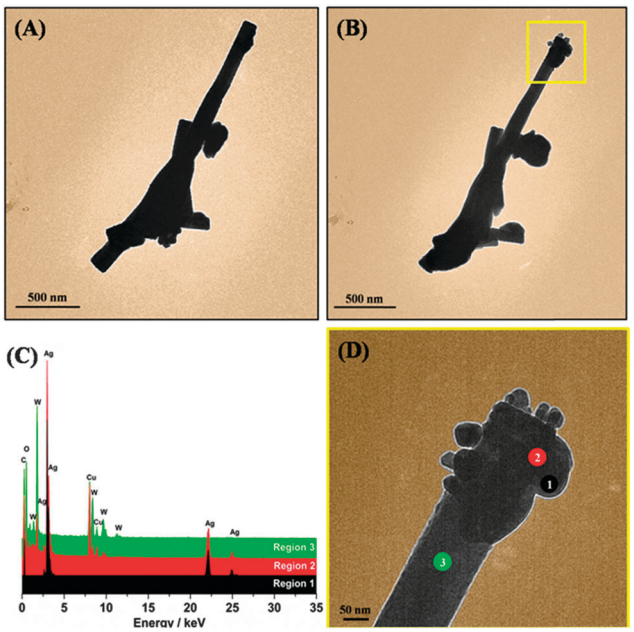

Fig. 5 TEM images of α-Ag_2WO_4 at (A) time zero and (B) after 5 minutes of exposure. (C) EDS spectra of the three regions, corresponding to points 1, 2 and 3, respectively, are depicted in (D).

Table 1 Ag and W relationship shown by EDS

Points	Ag (%)	W (%)
1	100	0
2	92.50	7.49
3	3.1	96.9

induces the presence of Ag defects inside the α-Ag_2WO_4 material and this semiconductor changes from an n to a p type.

Adsorption and absorption of electrons by the semiconductor Ag_2WO_4 followed by removal of silver causes distortion and breaking of the crystal symmetry. This physico-chemical effect produces the polarization between the clusters that makes the population of electronic excited states easy. These electrons reduce $[AgO_x]\left[V'_{Ag}\cdot O_x\right]$ and Ag^0, but are not energetic enough to reduce $[WO_6]^x$ clusters. The cluster-to-cluster charge transfer in α-$Ag_{2-x}WO_4$ crystals containing more than one kind of cluster is characterized by excitations involving electronic transitions from one cluster to another cluster. Therefore, these clusters have favorable conditions to promote the charge transfer process from $\left[V'_{Ag}\cdot O_x\right]$ clusters to $[AgO_x]$ clusters. This electronic transition between clusters probably occurs when α-$Ag_{2-x}WO_4$ microcrystals with distorted clusters are able to absorb electrons with a quantum confinement effect associated with electron reduction of silver clusters.

Ag nanoparticles emerge from the structure of α-$Ag_{2-x}WO_4$ and xAg^0. Collective plasmon excitations provide a connection between the semiconductor and Ag nanoparticles resulting in an increase of silver nanowire carriers, *i.e.* these emerging nanowires have a high defect density and the interactions at both intermediate and short ranges result in a dynamic equilibrium of formation of unstable clusters which leave the surface of the nanowires, forming clusters. This coupling semiconductor–metal-cluster opens the perspective of a new phenomenon of nature involving the effect of quantum confinement on plasmon resonance, *i.e.*, an optical signature nanoscale produced by charge carriers.

Bulk calculations

The α-Ag_2WO_4 bulk structure was calculated under full structural relaxation, which allowed for changes in the lattice parameters and the internal atomic positions. The calculated cell parameters were a = 11.234 Å, b = 12.574 Å and c = 5.812 Å which compare well with experimental values.[45,63] α-Ag_2WO_4 crystals belong to an orthorhombic structure with a space group of $Pn2n$, with a point-group $C_{2v}^{(10)}$ symmetry.[73] The bulk structure is formed by clusters of $[WO_6]$ and $[AgO_y]$ (y = 2, 4, 6 and 7).

(100) surface

The difference between surface and bulk properties is linked to the role of dimensionality, and we have studied the (100) surface, which is the most stable one. This surface is modelled using supercells with surface parameters of 11.624 × 12.574 Å. In order to test the reproducibility of results with respect to the slab thickness, we chose two different slab sizes of 3 and 6 layers resulting in systems with 84 and 168 atoms, respectively. The vacuum distance in this direction was set to 14 Å, which is large enough to avoid the interaction between the surface and its images. Once the supercell was created, all further relaxation processes were carried out allowing for the internal atomic positions to relax without changing the lattice parameters.

When cleaving the crystal, the coordination number of the surface atoms changes from the bulk situation. Thus, the W atoms change to a tetrahedral coordination, whereas the Ag atoms are found with coordination numbers of 4 and 6. The presence of these under-coordinated atoms modifies the electronic structure and distinguishes the surface from their bulk counterparts because of the bond contraction and bond energy elevation induced by atomic under-coordination. *Ab initio* molecular dynamics simulations of both slab models show that this oxide surface made of under-coordinated Ag atoms is suitable to undergo delicate structural rearrangements even at ambient temperature. The optimization process for both slabs leads to structures with some slight differences (see Fig. 6). However, and more importantly, the coordination number of all Ag atoms is preserved in both models, and the structural environment of each Ag atom can be considered approximately equivalent in both models. There are eight surface Ag atoms, which are arranged in four different arrangements. Ag-1 and Ag-2 are the outermost external Ag atoms and are four-fold coordinated. Ag-3 and Ag-4 are also four-fold coordinated, but they are in more internal positions. The next Ag atoms are even further into the slab and they are all six-fold coordinated. Only the smallest supercell model was used for performing the

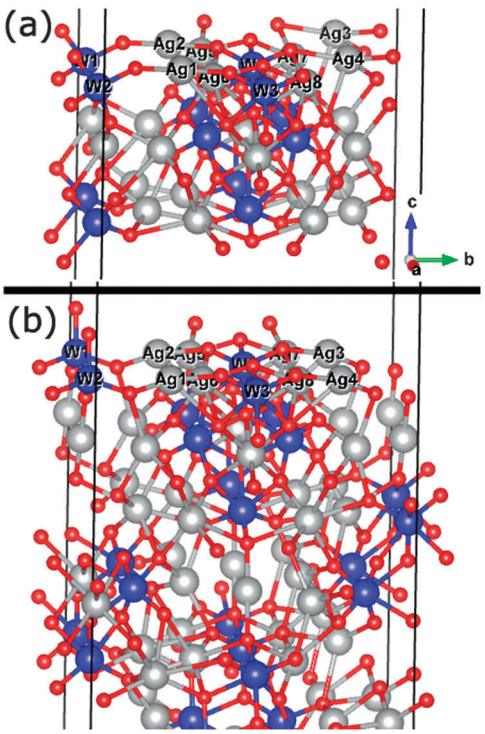

Fig. 6 Relaxed slab models for the (100) surface. (a) 3-Layer and (b) 6-layer models.

calculations that are described next, because the use of the 6-layer model would be too computationally demanding.

The mechanism of surface Ag nucleation induced by the electron injection starts from the presence of Ag adatoms on the surface. These reduced adatoms diffuse from the bulk material when hit by the electron bombardment. Presumably, the outermost external atoms would be more easily removed and would initiate the process. Geometry optimization of the system was done when each Ag atom is displaced to a higher Z coordinate outside the surface. There are no stable situations for the Ag-01, Ag-02, Ag-05, Ag-06 atoms and they were put back to the original positions. Conversely, the system is energetically favored at 0.25 eV when Ag-03 and Ag-04 are in external sites. In a similar way, the system is stabilized at 0.52 eV when Ag-07 and Ag-08 move outward, but a considerable surface rearrangement occurs simultaneously. We have computed the energy barrier for the diffusion process of Ag-03 and Ag-04 by means of the NEB method.

Fig. 7 shows the structures of the NEB evolution along the reaction coordinate (RC) from the initial position RC-00 (a) up to the final position RC-05 (f). Also, the energy profile along the reaction coordinate is depicted in the central plot. It corresponds basically to the movement of the Ag atom from the relaxed surface (RC-00) to the optimized situation when the atom is on the outer site (RC-05), which corresponds to a displacement of 0.65 Å. It can be seen that the energy cost is only around 0.10 eV, a low energy barrier, which makes this Ag surface atom very mobile and a good candidate to exit the surface and initiate the metal nucleation process.

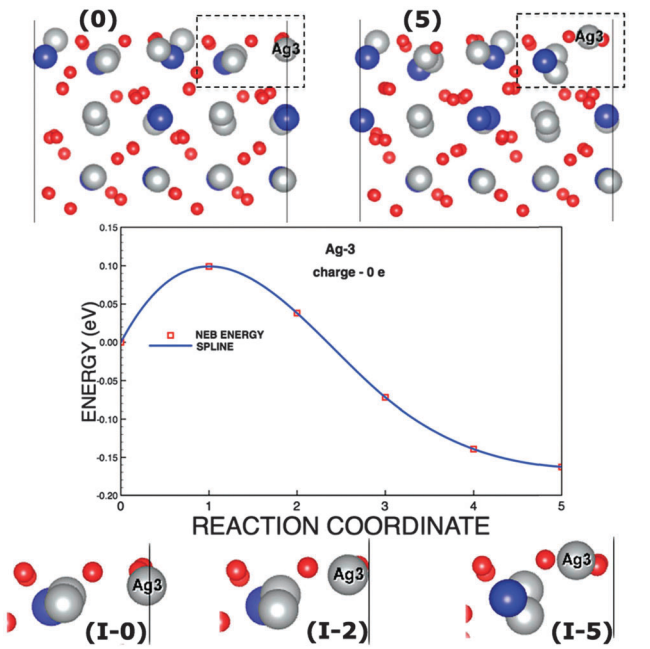

Fig. 7 Energy profile and structures obtained from a NEB calculation. The top two images labeled (0) and (5) are the initial and final structures, respectively. Insets of these structures and other intermediates along the reaction coordinate are labeled as (I-0), (I-5) and (I-2), respectively. The graph shows the energy profile along the reaction coordinate displaying a small barrier of 0.10 eV.

Although these Ag-3 and Ag-4 surface atoms appear to be very mobile, the charge effect provided by irradiation further helps this process. In order to verify this effect, the electron absorption process on the surface structure was also investigated. 1 to 3 electrons were added and relaxation of the surface clusters was analyzed. Fig. 8 shows how the Z coordinates of the surface Ag atoms change for each charge addition. It can be seen that as the number of injected electrons increases, the Ag-3 and Ag-4 atoms move outward whereas the positions of the other atoms do not significantly change.

This result indicates that excess electrons favor Ag-3 and Ag-4 atoms to move to the outermost external sites. To confirm this behavior, NEB calculations have been used to estimate the energy barrier for diffusion of these atoms when one electron is added into the system. Fig. 9 shows the diffusion energy profile and demonstrates that it is a non-barrier pathway. The small barrier presented (see Fig. 7) in the diffusion process (red squares) changes to a barrierless profile (red circles) upon charging the system with one electron. Therefore, these charge injection effects favor the escape of Ag atoms to form new Ag structures, nanowires and clusters as observed in the experiments presented in this article and in previous publications.[49–52]

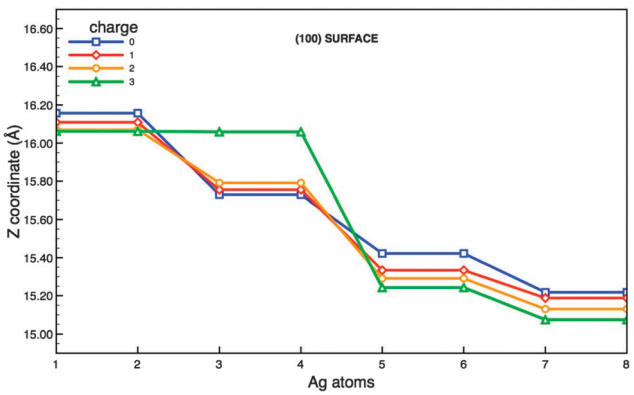

Fig. 8 Z coordinates of the surface Ag atoms for each charge addition.

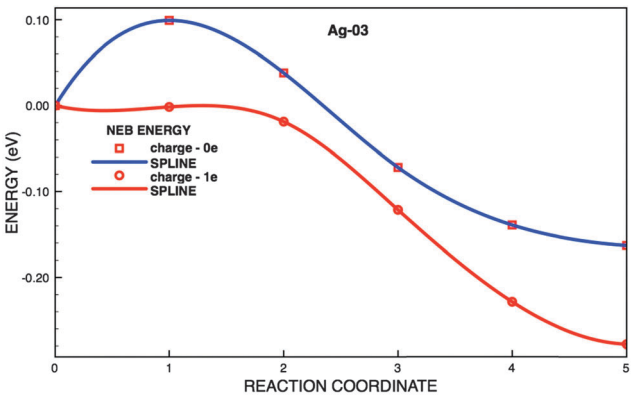

Fig. 9 Energy profiles for the diffusion process of the Ag-03 atom in a neutral system (blue line and red squares) when one electron is added into the system (red circles).

5. Conclusions

In this study, α-Ag_2WO_4 samples were grown using a simple co-precipitation method. How the *in situ* Ag nanoparticle growth and morphological evolution on α-Ag_2WO_4 take place during electron beam irradiation has been analyzed. These events were directly monitored in real-time using *in situ* TEM and FE-SEM spectroscopic techniques and first principle calculations to provide a deeper insight and understanding of these processes in individual nanostructures at the atomic to nanoscale levels.

This promising methodology was demonstrated based on the combination of experiments and calculations, through their application to a long-standing challenging problem, namely, the Ag nanoparticle growth and morphological evolution on α-Ag_2WO_4 during electron beam irradiation. The results of the present study can be summarized as follows: (i) the formation of Ag nanoparticles takes place on the α-Ag_2WO_4 surface after a few seconds of exposure to an electron beam and is not dependent on the electron beam voltage. (ii) The sizes of Ag nanoparticles cover a wide range of values, with most of the Ag particles being 20–40 nm in size. (iii) First principle calculations of the (100) surface, as the most stable of α-Ag_2WO_4, allow a detailed analysis of the Ag active centers. (iv) The theoretical results point out that Ag-3 and Ag-4 four-fold coordinated centers, located in the sub-surface, are the most energetically favorable to suffer the diffusion process to form metallic Ag. (v) *Ab initio* molecular dynamics simulations and NEB calculations point out that the injection of electrons decreases the activation barrier for the diffusion process of these Ag centers.

The present study has drawn a fundamental physical picture for understanding electron-enhanced activity, and the data reveal real-time insights into the activation of α-Ag_2WO_4 by the electron beam and constitutes a new example of how and where silver nanoparticles are formed by modifying the electron density and opens the door to future transformations and applications.

Acknowledgements

The authors are grateful to Prometeo/2009/053 (Generalitat-Valenciana), Ministerio de Economia y Competitividad (Spain), CTQ2012-36253-C03-02, Spanish Brazilian program (PHB2009-0065-PC), FAPESP (Project 2013/07296-2) (Project 2012/14468-1) (Project 2010/16970-0), grant (2013/02032-7), CAPES and CNPq (Project 573636/2008-7, Grant 150753/2013-6) and CAPES (Project 088/2013) for financially supporting this research. Most of the calculations were performed using IFGW-UNICAMP computer facilities and the National Center for High Performance Computing in São Paulo (CENAPAD-SP). We also acknowledge the Servei Informática, Universitat Jaume I, for the generous allotment of computer time.

Notes and references

1 N. de Jonge and F. M. Ross, *Nat. Nanotechnol.*, 2011, **6**(11), 695–704.
2 T. J. Woehl, J. E. Evans, L. Arslan, W. D. Ristenpart and N. D. Browning, *ACS Nano*, 2012, **6**(10), 8599–8610.
3 R. F. Egerton, P. Li and M. Malac, *Micron*, 2004, **35**(6), 399–409.
4 L. R. Parent, D. B. Robinson, T. J. Woehl, W. D. Ristenpart, J. E. Evans, N. D. Browning and I. Arslan, *ACS Nano*, 2012, **6**(4), 3589–3596.
5 T. J. Woehl, K. L. Jungjohann, J. E. Evans, I. Arslan, W. D. Ristenpart and N. D. Browning, *Ultramicroscopy*, 2013, **127**, 53–63.
6 E. J. R. Vesseur, J. Aizpurua, T. Coenen, A. Reyes-Coronado, P. E. Batson and A. Polman, *MRS Bull.*, 2012, **37**(8), 752–760.
7 D. B. C. Williams and C. B. Carter, *Transmission Electron Microscopy: A Textbook for Materials Science*, Springer, Berlin, 2nd edn, 2009.
8 A. Yurtsever, M. Couillard and D. A. Muller, *Phys. Rev. Lett.*, 2008, **100**(21), 217402.
9 S. B. Simonsen, I. Chorkendorff, S. Dahl, M. Skoglundh, J. Sehested and S. Helveg, *J. Am. Chem. Soc.*, 2010, **132**(23), 7968–7975.
10 J. E. Evans, K. L. Jungjohann, N. D. Browning and I. Arslan, *Nano Lett.*, 2011, **11**(7), 2809–2813.
11 Y. Liu, K. Tai and S. J. Dillon, *Chem. Mater.*, 2013, **25**(15), 2927–2933.
12 H. Zheng, R. K. Smith, Y.-w. Jun, C. Kisielowski, U. Dahmen and A. P. Alivisatos, *Science*, 2009, **324**(5932), 1309–1312.
13 E. U. Donev and J. T. Hastings, *Nano Lett.*, 2009, **9**(7), 2715–2718.
14 Y. Liu, X. Chen, K. W. Noh and S. J. Dillon, *Nanotechnology*, 2012, **23**(38), 385302.
15 G. Schardein, E. U. Donev and J. T. Hastings, *Nanotechnology*, 2011, **22**(1), 015301.
16 K. W. Noh, Y. Liu, L. Sun and S. J. Dillon, *Ultramicroscopy*, 2012, **116**, 34–38.
17 S. E. Habas, H. Lee, V. Radmilovic, G. A. Somorjai and P. Yang, *Nat. Mater.*, 2007, **6**(9), 692–697.
18 F. Kim, S. Connor, H. Song, T. Kuykendall and P. D. Yang, *Angew. Chem., Int. Ed.*, 2004, **43**(28), 3673–3677.
19 B. Lim, Y. Xiong and Y. Xia, *Angew. Chem., Int. Ed.*, 2007, **46**(48), 9279–9282.
20 T. K. Sau and A. L. Rogach, *Adv. Mater.*, 2010, **22**(16), 1781–1804.
21 D. Seo, C. I. Yoo, J. C. Park, S. M. Park, S. Ryu and H. Song, *Angew. Chem., Int. Ed.*, 2008, **47**(4), 763–767.
22 A. R. Tao, S. Habas and P. Yang, *Small*, 2008, **4**(3), 310–325.
23 N. Tian, Z.-Y. Zhou, S.-G. Sun, Y. Ding and Z. L. Wang, *Science*, 2007, **316**(5825), 732–735.
24 B. Wiley, Y. G. Sun, B. Mayers and Y. N. Xia, *Chem. – Eur. J.*, 2005, **11**(2), 454–463.
25 Q. Zhang, J. Xie, J. Yang and J. Y. Lee, *ACS Nano*, 2009, **3**(1), 139–148.
26 P. E. Batson, A. Reyes-Coronado, R. G. Barrera, A. Rivacoba, P. M. Echenique and J. Aizpurua, *Nano Lett.*, 2011, **11**(8), 3388–3393.
27 F. J. Garcia de Abajo, *Rev. Mod. Phys.*, 2010, **82**(1), 209–275.
28 S. W. Chee, S. Sivaramakrishnan, R. Sharma and J.-M. Zuo, *Microsc. Microanal.*, 2011, **17**(2), 274–278.
29 F. Tao and M. Salmeron, *Science*, 2011, **331**(6014), 171–174.

30 H.-G. Liao, K. Niu and H. Zheng, *Chem. Commun.*, 2013, **49**(100), 11720–11727.
31 J. M. Yuk, J. Park, P. Ercius, K. Kim, D. J. Hellebusch, M. F. Crommie, J. Y. Lee, A. Zettl and A. P. Alivisatos, *Science*, 2012, **336**(6077), 61–64.
32 H. G. Liao, L. K. Cui, S. Whitelam and H. M. Zheng, *Science*, 2012, **336**(6084), 1011–1014.
33 P. Christopher, H. Xin and S. Linic, *Nat. Chem.*, 2011, **3**(6), 467–472.
34 S. Linic, P. Christopher and D. B. Ingram, *Nat. Mater.*, 2011, **10**(12), 911–921.
35 M. Xiao, R. Jiang, F. Wang, C. Fang, J. Wang and J. C. Yu, *J. Mater. Chem. A*, 2013, **1**(19), 5790–5805.
36 X. Zhang, Y. L. Chen, R.-S. Liu and D. P. Tsai, *Rep. Prog. Phys.*, 2013, **76**(4), 046401.
37 W. H. Hung, M. Aykol, D. Valley, W. Hou and S. B. Cronin, *Nano Lett.*, 2010, **10**(4), 1314–1318.
38 D. B. Ingram and S. Linic, *J. Am. Chem. Soc.*, 2011, **133**(14), 5202–5205.
39 S. Navalon, M. de Miguel, R. Martin, M. Alvaro and H. Garcia, *J. Am. Chem. Soc.*, 2011, **133**(7), 2218–2226.
40 S.-i. Naya, A. Inoue and H. Tada, *J. Am. Chem. Soc.*, 2010, **132**(18), 6292–6293.
41 A. Primo, T. Marino, A. Corma, R. Molinari and H. Garcia, *J. Am. Chem. Soc.*, 2011, **133**(18), 6930–6933.
42 E. Thimsen, F. Le Formal, M. Graetzel and S. C. Warren, *Nano Lett.*, 2011, **11**(1), 35–43.
43 I. Thomann, B. A. Pinaud, Z. Chen, B. M. Clemens, T. F. Jaramillo and M. L. Brongersma, *Nano Lett.*, 2011, **11**(8), 3440–3446.
44 D. Tsukamoto, Y. Shiraishi, Y. Sugano, S. Ichikawa, S. Tanaka and T. Hirai, *J. Am. Chem. Soc.*, 2012, **134**(14), 6309–6315.
45 C. Gomes Silva, R. Juarez, T. Marino, R. Molinari and H. Garcia, *J. Am. Chem. Soc.*, 2011, **133**(3), 595–602.
46 S. Mukherjee, F. Libisch, N. Large, O. Neumann, L. V. Brown, J. Cheng, J. B. Lassiter, E. A. Carter, P. Nordlander and N. J. Halas, *Nano Lett.*, 2013, **13**(1), 240–247.
47 Z. Zhao and M. A. Carpenter, *J. Phys. Chem. C*, 2013, **117**(21), 11124–11132.
48 E. Longo, L. S. Cavalcante, D. P. Volanti, A. F. Gouveia, V. M. Longo, J. A. Varela, M. O. Orlandi and J. Andres, *Sci. Rep.*, 2013, **3**, 1676.
49 J. Andrés, L. Gracia, P. Gonzalez-Navarrete, V. M. Longo, W. Avansi Jr., D. P. Volanti, M. M. Ferrer, P. S. Lemos, F. A. L. Porta, A. C. Hernandes and E. Longo, *Sci. Rep.*, 2014, **5**, 5391.
50 E. Longo, D. P. Volanti, V. M. Longo, L. Gracia, I. C. Nogueira, M. A. P. Almeida, A. N. Pinheiro, M. M. Ferrer, L. S. Cavalcante and J. Andrés, *J. Phys. Chem. C*, 2014, **118**, 1229–1239.
51 V. M. Longo, C. C. D. Foggi, M. M. Ferrer, A. F. Gouveia, R. S. André, W. Avansi, C. E. Vergani, A. L. Machado, J. Andrés, L. S. Cavalcante, A. C. Hernandes and E. Longo, *J. Phys. Chem. A*, 2014, **118**, 5769–5778.
52 L. F. da Silva, A. C. Catto, W. Avansi, Jr., L. S. Cavalcante, J. Andres, K. Aguir, V. R. Mastelaro and E. Longo, *Nanoscale*, 2014, **6**(8), 4058–4062.
53 S. J. L. Billinge and I. Levin, *Science*, 2007, **316**(5824), 561–565.
54 G. Kresse and J. Furthmuller, *Comput. Mater. Sci.*, 2007, **6**(1), 15–50.
55 G. Kresse and J. Furthmuller, *Phys. Rev. B: Condens. Matter Mater. Phys.*, 1996, **54**(16), 11169–11186.
56 G. Kresse and J. Hafner, *Phys. Rev. B: Condens. Matter Mater. Phys.*, 1993, **47**(1), 558–561.
57 P. E. Blochl, *Phys. Rev. B: Condens. Matter Mater. Phys.*, 1994, **50**(24), 17953–17979.
58 G. Kresse and D. Joubert, *Phys. Rev. B: Condens. Matter Mater. Phys.*, 1999, **59**(3), 1758–1775.
59 P. E. Blöchl, O. Jepsen and O. K. Andersen, *Phys. Rev. B: Condens. Matter Mater. Phys.*, 1994, **49**(23), 16223–16233.
60 J. P. Perdew, K. Burke and M. Ernzerhof, *Phys. Rev. Lett.*, 1996, **77**(18), 3865–3868.
61 J. P. Perdew, J. A. Chevary, S. H. Vosko, K. A. Jackson, M. R. Pederson, D. J. Singh and C. Fiolhais, *Phys. Rev. B: Condens. Matter Mater. Phys.*, 1992, **46**(11), 6671–6687.
62 H. Jonsson, G. Mills, K. W. Jacobsen and B. J. Berne, *Classical and Quantum Dynamics in Condensed Phase Simulations*, World Scientific, Singapore, 1998.
63 L. S. Cavalcante, M. A. P. Almeida, W. Avansi, Jr., R. L. Tranquilin, E. Longo, N. C. Batista, V. R. Mastelaro and M. Siu Li, *Inorg. Chem.*, 2012, **51**(20), 10675–10687.
64 T. George, S. Joseph and S. Mathew, *Pramana*, 2005, **65**(5), 793–799.
65 B. Hu, L.-H. Wu, S.-J. Liu, H.-B. Yao, H.-Y. Shi, G.-P. Li and S.-H. Yu, *Chem. Commun.*, 2010, **46**(13), 2277–2279.
66 X. Wang, S. Li, H. Yu and J. Yu, *J. Mol. Catal. A: Chem.*, 2011, **334**(1–2), 52–59.
67 X. J. Cui, S. H. Yu, L. L. Li, L. Biao, H. B. Li, M. S. Mo and X. M. Liu, *Chem. – Eur. J.*, 2004, **10**(1), 218–223.
68 J. A. Faucheaux, A. L. D. Stanton and P. K. Jain, *J. Phys. Chem. Lett.*, 2014, **5**(6), 976–985.
69 S. A. Maier, *Plasmonics: Fundamentals and Applications*, Springer, New York, 2007.
70 C. F. H. Bohren and D. R. Huffman, *Absorption and Scattering of Light by Small Particles*, Wiley, New York, 1998.
71 I. Kriegel, J. Rodriguez-Fernandez, A. Wisnet, H. Zhang, C. Waurisch, A. Eychmueller, A. Dubavik, A. O. Govorov and J. Feldmann, *ACS Nano*, 2013, **7**(5), 4367–4377.
72 A. M. Schimpf, N. Thakkar, C. E. Gunthardt, D. J. Masiello and D. R. Gamelin, *ACS Nano*, 2014, **8**(1), 1065–1072.
73 P. M. Skarstad and S. Geller, *Mater. Res. Bull.*, 1975, **10**(8), 791–799.